Available online at www.sciencedirect.com
SCIENCE DIRECT®
Earth and Planetary Science Letters 232 (2005) 259–272
EPSL
www.elsevier.com/locate/epsl

# Deep structure and seismic anisotropy beneath the East Pacific Rise

Yu J. Gu[a,*], Arthur L. Lerner-Lam[b], Adam M. Dziewonski[c], Göran Ekström[c]

[a]Lamont-Doherty Earth Observatory, Columbia University, New York, NY 10964, USA
[b]Department of Earth and Environmental Sciences, Columbia University, New York, NY 10964, USA
[c]Department of Earth and Planetary Sciences, Harvard University, 20 Oxford Street, Cambridge, MA 02138, USA

Received 1 July 2004; received in revised form 6 January 2005; accepted 18 January 2005
Available online 7 March 2005
Editor: K. Farley

**Abstract**

Seismic velocities in the upper mantle beneath mid-ocean ridges are known to exhibit anisotropy, especially at depths shallower than 200 km. In this study, we present evidence for deeper anisotropy beneath fast-spreading ridges based on simultaneous inversion of body wave travel times, waveforms, and surface wave phase velocities. The 'vertical' ($B_{SV}$) shear wave speed is systematically faster (by more than 2%) than the 'horizontal' ($B_{SH}$) one at depths of 200–300 km beneath the East Pacific Rise, a result that is consistent with vertical alignment of the fast crystallographic axis of olivine. This anomaly is especially coherent beneath the northern East Pacific Rise, where the observations also support the presence of a modest mantle reflector near 260-km depth. The anisotropy may be associated with deep vertical flow or finite strain, and the presence of this reflector could signal a rheological transition near the bottom of the asthenosphere, reflecting changes in flow direction, development of partial melt, or the persistence of a deep pre-existing strain regime.


*Keywords:* Deep structure; Seismic anisotropy; East Pacific Rise

## 1. Introduction

The conventional description of rigid oceanic lithosphere moving coherently over weak asthenosphere is supported by long-standing seismological observations of a high-velocity oceanic lid overlying a deeper low-velocity zone [1–3]. Pure-path inversions of surface-wave phase velocities and tomographic images of P- and S-wave speeds provide different levels of details but consistently show that oceanic crust thickens with increasing age. This is commonly interpreted in terms of a thermal regime dominated by the conductive cooling of the spreading oceanic plate. This simple thermal model is incomplete in the vicinity of mid-ocean ridges, however, as dynamic mechanisms such as hydrothermal circulation, mag-

* Corresponding author. Now at: Department of Physics, University of Alberta, 535A Avadh Bhatia Physics Laboratory, Edmonton, Canada T6G2J1. Tel.: +1 780 492 2292; fax: +1 780 492 0714.
*E-mail addresses:* ygu@ualberta.ca (Y.J. Gu), lerner@ldeo.columbia.edu (A.L. Lerner-Lam), dziewons@seismology.harvard.edu (A.M. Dziewonski), ekstrom@seismology.harvard.edu (G. Ekström).

0012-821X/$ - see front matter © 2005 Elsevier B.V. All rights reserved.
doi:10.1016/j.epsl.2005.01.019

magenesis, mass transport, and active/passive heat flow impart significant effects on the formation of oceanic lithosphere and organization of sea-floor spreading. Dynamic proxies obtained from seismological observations, such as shear wave anisotropy, impose direct constraints on the processes that culminate in sea floor spreading. When anisotropy is well resolved at depths in the upper mantle, it becomes possible to relate the organization of sea-floor spreading to larger-scale components of mantle convection. Such resolution is difficult, however, without access to regionally or locally targeted deployments of seismometers near ocean ridges, or through measurements of portions of the seismic wave field that are particularly sensitive to the upper mantle structure beneath ridges. This paper takes the latter approach.

The theory of seismic anisotropy is well established [4,5]. Finite strains or flow in the mantle are manifested in the lattice-preferred orientation (LPO) of anisotropic minerals such as olivine. The characterization of anisotropic wave speeds depends critically on the mineralogy, temperature, and, potentially, the presence of water [3,6–9]. Recent studies involving shear wave splitting [10–18] and global inversions [19,20] suggest that both 'fossil' and present-day, finite-strain-induced anisotropy exist in the upper mantle and often correlate with past and ongoing plate motions. For example, Plomerova et al. [21] and Gung et al. [20] used the depth dependence of anisotropy within the oceanic upper mantle to argue for sub-horizontal asthenospheric flow beneath the vast areas of oceanic plates away from ridges and subduction zones.

However, the detailed relationship between plate motion and deep mantle flow is less clear at mid-ocean ridges, especially below 150 km. At depths shallower than 150 km, global surface wave studies using on-land recordings (e.g., [22]) and regional analyses of data recorded by ocean bottom seismometers [23] suggest 5–8% shear-wave anisotropy in the upper 100 km beneath the southern EPR. In the same region, Wolfe and Solomon [10] inferred two zones of anisotropy with depth from core phase splitting observations. They associated the shallower zone beneath the Pacific side of the EPR with spreading-induced flow and a deeper zone with return flow potentially originating from the Pacific Superswell. Using a global data set with limited horizontal and vertical resolutions, Montagner and Tanimoto [6] reported deep anisotropy at 200–300 km depths that they interpreted as representing vertical flow beneath the ridges. While these results brought important insights onto the thermal and dynamical regimes, it is difficult to constrain the multi-scale interactions beneath the ridge without self-consistent joint inversions that examine the tradeoffs among the heterogeneous data sets. In particular, it is unclear how to assess the joint resolution of these studies and vitiate discrimination of changes in anisotropy with depth.

In this study, we describe the results of a radially anisotropic study of broadband body and surface waves that propagate or reflect in the vicinity of mid-ocean ridges. Our method takes into account the effect of along-path variation in kernel sensitivity owing to ray direction. We invert for polarization (or transverse) anisotropy, with a vertical (radial) symmetry axis, and allow for a general parameterization of the anisotropic structure as a function of depth. Our results favor a transition of mantle flow from a deeper, dominantly vertical orientation to a horizontal orientation at shallower depths. We also find evidence for a seismic discontinuity/reflector at 260-km depth beneath the EPR, coinciding with the approximate bottoming depth of the anisotropic regime. The significance of these findings and implications for mantle convection will be discussed.

## 2. Data and method

### 2.1. Data description

Given the relative paucity of direct seafloor observations of regional waveforms, we have aimed to increase the vertical resolution of our inversions by including travel times and waveforms from body wave phases with multiple reflections (also termed "mantle waves" or higher-mode surface waves) in the vicinity of the EPR. Our data set comprises more than 33,000 waveforms and 110,000 travel time measurements from $M_w$>5 earthquakes during the past decade, compiled by the Harvard Seismology Group (see Table 1). We also include the measurements of

Table 1
Data sets used in the anisotropic inversion

| Waveform/surface wave dispersion | | Absolute/differential travel time | |
|---|---|---|---|
| Body wave ($T$>45 s, V) | 6606 | *S* | 26,462 |
| Body wave ($T$>45 s, T) | 5729 | *SS* | 11,410 |
| Mantle wave ($T$>85 s, V) | 3523 | *ScS* | 4422 |
| Mantle wave ($T$>85 s, T) | 2840 | *SS–S* | 5124 |
| Mantle wave ($T$>135 s, V) | 3353 | *ScS–S* | 3567 |
| Mantle wave ($T$>135 s, T) | 2810 | *S–SKS* | 3550 |
| Mantle wave ($T$>200 s, V) | 3470 | *SKKS–SKS* | 2232 |
| Mantle wave ($T$>200 s, T) | 1880 | *SS–S670S* | 21,042 |
| Love wave (35–150 s) | 15,473–23,228 | *SS–S400S* | 21,042 |
| Rayleigh wave (135–150 s) | 28,457–37,739 | *S400S–S670S* | 17,271 |

$T$=period; V=vertical; T=transverse.

Rayleigh and Love wave phase velocity dispersion provided by Ekström et al. [22].

### 2.2. Parameterization and modeling strategy

Isotropic and anisotropic velocity variations are estimated using the inversion technique of Gu et al. [24]. The need for anisotropy is confirmed by successive inversions for velocity structure with different anisotropic parameterization [25], and the depth extent of anisotropy beneath 150 km is verified using a posteriori resolution tests. Our inversions are parameterized in terms of radial anisotropy (i.e., polarization anisotropy with a radial or vertical axis of symmetry). Such a parameterization is useful when the path coverage averages out azimuthal variations, a condition that is effectively achieved by the comprehensive data set used in this study.

Of the five elastic parameters normally required to parameterize transverse isotropy (commonly, A, C, N, L, and F) [3–5,26,27], our data set is primarily sensitive to the shear velocity terms N, L, and F. For transverse isotropy, SV and SH polarized shear waves travel at different velocities and both velocities vary as a function of the ray angle from vertical. We parameterize our inversions in terms of the velocities of horizontally traveling SV and SH waves, $B_{SV}$ and $B_{SH}$. Expressing the velocity as $V(\theta)$, where $\theta$ is the ray angle from vertical, we note that $B_{SV}=V_{SV}(90)=V_{SV}(0)=V_{SH}(0)$. In other words, for vertically traveling waves, both SH and SV polarized shear waves travel at the same speed, identical to the speed of horizontally traveling SV polarized shear waves.

Perturbations to $B_{SV}$ and $B_{SH}$ are often found by separate inversions of Rayleigh and Love wave data sets, respectively (see, for example, [19]). However, the mantle waves (higher-mode surface waves at low wavenumbers and frequencies) included in our study are sensitive to both $B_{SV}$ and $B_{SH}$, as depicted in Fig. 1. Thus our insistence on a joint inversion mandates that we use the full kernel representation, rather than separate inversions of $B_{SV}$ and $B_{SH}$ using polarized kernels. Such an approach automatically accounts for the variation of $B_{SV}$ and $B_{SH}$ sensitivity along the ray path of a multiply reflected mantle wave and minimizes unmodeled correlations between them.

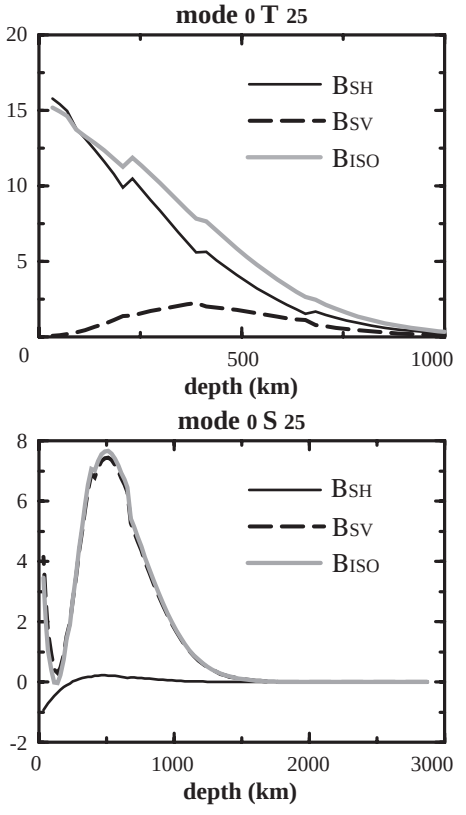


Fig. 1. Depth sensitivity kernels for toroidal mode ${}_0T_{25}$ (top) and spheroidal mode ${}_0S_{25}$, (bottom), computed using PREM [4]. $B_{ISO}$ represents the mode sensitivity to the isotropic shear speed. Toroidal modes are highly sensitive to $B_{SH}$, and spheroidal modes are dominated by $B_{SV}$. $B_{ISO}$ represents the isotropic wave speed.

For a given mode type (i.e., toroidal or spheroidal), the sensitivities to $B_{SV}$ and $B_{SH}$ speeds are nonzero and vary in a complex manner as a function of depth (see Fig. 1). The sample ray-theoretical travel time kernels account for both $B_{SV}$ and $B_{SH}$ contributions in response to wave polarization and propagation directions (Fig. 2). This is especially important for SH-polarized waves near the source and the receiver, where the wave vectors are close to vertical, and the turning points where the wave vectors are perpendicular to the symmetry axis. This implies that the approach to divide the data into $B_{SV}$- and $B_{SH}$-sensitive subsets is, strictly speaking, inaccurate. SV polarized waves are only sensitive to $B_{SV}$ but the sensitivity varies as a function of ray propagation angle (see Fig. 2, bottom right).

In addition, the weak dependence on compressional wave speeds is incorporated into our inversion through an implicit scaling relationship $\delta V_P/V_P=0.55$ $\delta V_S/V_S$ in the calculation of the mantle waveform kernels. Varying the proportionality constant between 0.0 and 1.0 does not affect the shear wave inversion results significantly [19,20]. The deeper variations in vertical and horizontal wave speeds are primarily

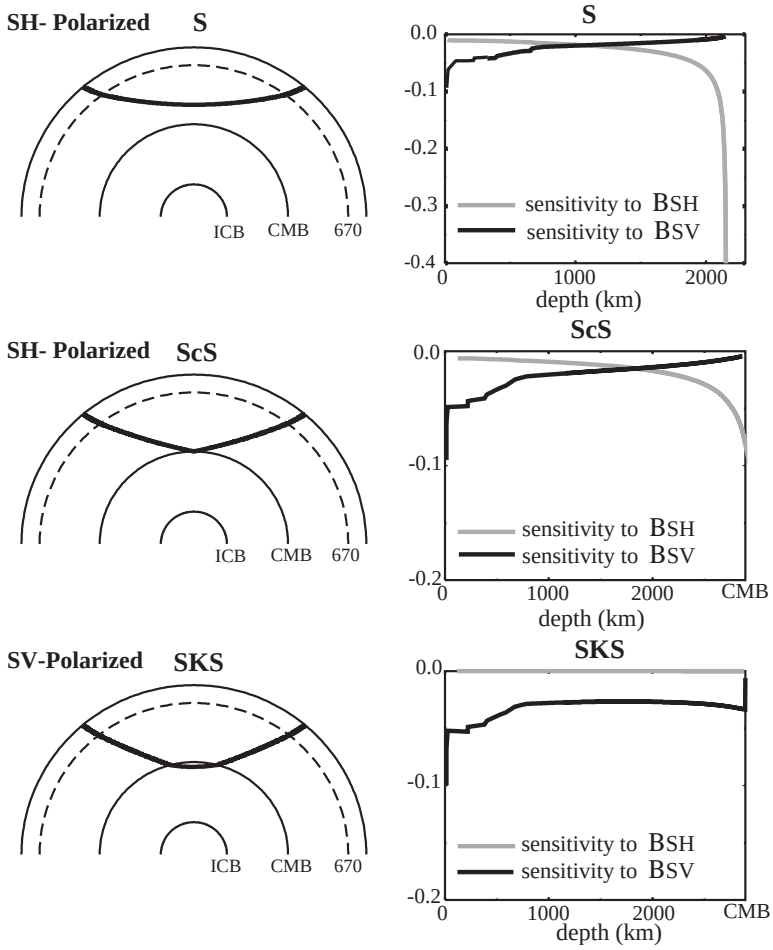


Fig. 2. Sample travel time sensitivity kernels showing the first contributing ray leg. These are ray-theoretical kernels that consider both the polarization of the waves and the propagation directions. A transversely polarized wave (e.g., *S*) is primarily sensitive to $B_{SV}$ near the surface when the ray is traveling nearly vertically. SV polarized waves are only sensitive to $B_{SV}$ wave speed, and the sensitivity is dominated by the direction of the wave vector.

constrained by Love and Rayleigh waves and very long-period, reverberative body waves.

### 2.3. More on inversion method

Following Gung et al. [20], we invert simultaneously for Voigt average velocity perturbations ($0.33\delta B_{SH}/B_{SH}+0.67\delta B_{SV}/B_{SV}$) and the anisotropic parameter ($\delta B_{SV}/B_{SV}-\delta B_{SH}/B_{SH}$). This approach provides a structure to balance the differences in the path coverage of Love and Rayleigh wave data. Through perturbations to $B_{SV}$ and $B_{SH}$, we are able to choose regularization constants that smooth the results by damping the sparser coverage with constraints from the denser coverage. The style of inversion differs significantly from earlier anisotropic shear wave inversions [3,6,19] that relied on different regularization constants for separate polarizations.

We expand the lateral variations of velocity and discontinuity topography using spherical B-splines with 362 nodes uniformly distributed on a sphere. The radial variations are represented using 14 B-splines, six in the upper mantle and eight in the lower mantle, as in [25]. We express a shear velocity perturbation $\delta B_x$ ($x$ represents SH or SV) relative to reference velocity $B_{x0}$ as:

$$\frac{\delta B_x(r,\theta,\phi)}{B_{x0}(r,\theta,\phi)} = \sum_{ij} C_{ij} b_i(r) S_j(\theta,\phi),$$

where $C_{ij}$ is the unknown coefficient of a wave speed, $b_i(r)$ is the $i$th radial B-spline, $S_j(\theta,\phi)$ is the $j$th spherical B-spline, and $B_{x0}$ is the appropriate anisotropic PREM velocity [4]. In general, differences in the modeling results using local and global parameterizations (with comparable degrees of freedom) are relatively small [28]. Parameterization using local basis functions, however, enables the convenient computation and storage of sparse matrices. Prior to inversions, each data set is corrected for the effect of crust using CRUST-5.1 [29], as well as for topography and bathymetry. Our inversion regularizes toward both a smooth horizontal perturbation and minimum model, with smoothing and size norms calculated for linear combinations of the velocity perturbations as defined above.

The inversion minimizes the least squares misfit between observed and predicted travel times, dispersion, and waveforms. Since true observational and modeling errors are largely unknown, the different data sets are combined using weighting coefficients determined empirically. The cumulative sensitivity (Fig. 3) of different data sets, averaged over all mantle depths, varies as a function of wave type and size of the data set. For example, Rayleigh and Love wave dispersion measurements greatly improve the upper mantle resolution of 'vertical' and 'horizontal' wave speeds, respectively. The mantle and body wave waveforms contribute slightly smaller but significant constraints in the upper mantle. The travel times of *S* and *SS*, measured on the transverse component, are functions of both velocities, whereas *SKS* is exclusively sensitive to $B_{SV}$. The diversity of the data set greatly enhances azimuthal averaging, justifying the parameterization of the model in terms of transverse isotropy. Anisotropic inversions reduce the variance

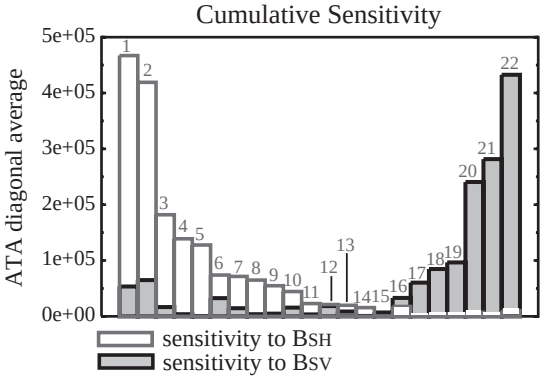


Fig. 3. Cumulative $B_{SH}$ and $B_{SV}$ sensitivities averaged over all mantle depths. These values are computed from the diagonal averages of the inner product matrices ($A^TA$). The waveform data set includes both mantle ('M') and body ('B') waves. Two subsets compiled for different periods will be referred to as 'old' (1980–1989) and 'new' (1990–2003). The numbers represent: 1=*SS*, 2=*S*, 3=*SS–S*, 4=waveform (new, M, *T*>85 s, T), 5=love, 6=*SS–S670S*, 7=*ScS–S*, 8=waveform (old, M, *T*>135 s, T), 9=waveform (old, B, *T*>45 s, T), 10=*S–SKS*, 11=waveform (new, B, *T*>45 s, T), 12=*SS–S400S*, 13=*S400S–S670S*, 14=waveform (new, M, *T*>200 s, T), 15=*SKKS–SKS*, 16=*ScS*, 17=waveform (new, M, *T*>200 s, V), 18=waveform (old, B, *T*>45 s, V), 19=waveform (new, B, *T*>45 s, V), 20=waveform (old, M, *T*>135 s, V), 21=Rayleigh, 22=waveform (new, M, *T*>85 s, V). *T* represents the wave period, and T and V represent transverse and vertical components, respectively. The only data set that does not constrain $B_{SH}$ is *SKS* since it is exclusively measured on the vertical component (P–SV) seismograms.

of fit by approximately 10% relative to the best-fit isotropic model, with significant improvements obtained for long-period travel times.

## 3. Model results: deep asthenospheric anomalies beneath EPR

### 3.1. Resolution and radial anisotropy

Fig. 4 shows the relative $B_{SH}$ and $B_{SV}$ perturbations to the laterally homogeneous anisotropic reference model, PREM [4], between 200 km and 400 km. The third column shows the anisotropic perturbation, which we define by their difference $(\delta B_{SV}-\delta B_{SH})/B_0$; only one reference speed is needed for the depths shown in Fig. 4 since PREM is isotropic beneath 220 km. The large-scale patterns of anisotropy are generally consistent with [19,20]: while lateral changes to $B_{SV}$ and $B_{SH}$ tend to track each other in most areas of the upper mantle, with $B_{SH}$ being generally greater than $B_{SV}$, the anisotropic parameter changes sign at depths greater than ~180 km beneath the EPR. The strength of the relative anisotropy under the EPR (~2.5%) is at least comparable in size with that beneath the central Pacific and most continents, although of opposite sign.

The anomaly with respect to anisotropic PREM is the most pronounced beneath the northern EPR (Fig. 5a). Fig. 5b shows a cross section through the northern EPR, positioned near the Guatemala basin. A strong negative ($\delta\ln B_{SV}<\delta\ln B_{SH}$) anomaly is present above 100 km, with the maximum variation near 50-km depth (Fig. 5c) and resolved lateral dimensions of approximately 2000 km (east–west) by 4000 km (north–south). This negative anomaly spans nearly the entire Cocos plate and the strength decreases with depth until the difference between $B_{SV}$ and $B_{SH}$ changes sign near 150 km. Below 150 km, the positive ($\delta\ln B_{SV}>\delta\ln B_{SH}$) anisotropy increases gradually and reaches its maximum amplitude of 2.5% at 230 km (see Fig. 5c). The fast vertical pattern spans 2500 km laterally and more than 150 km

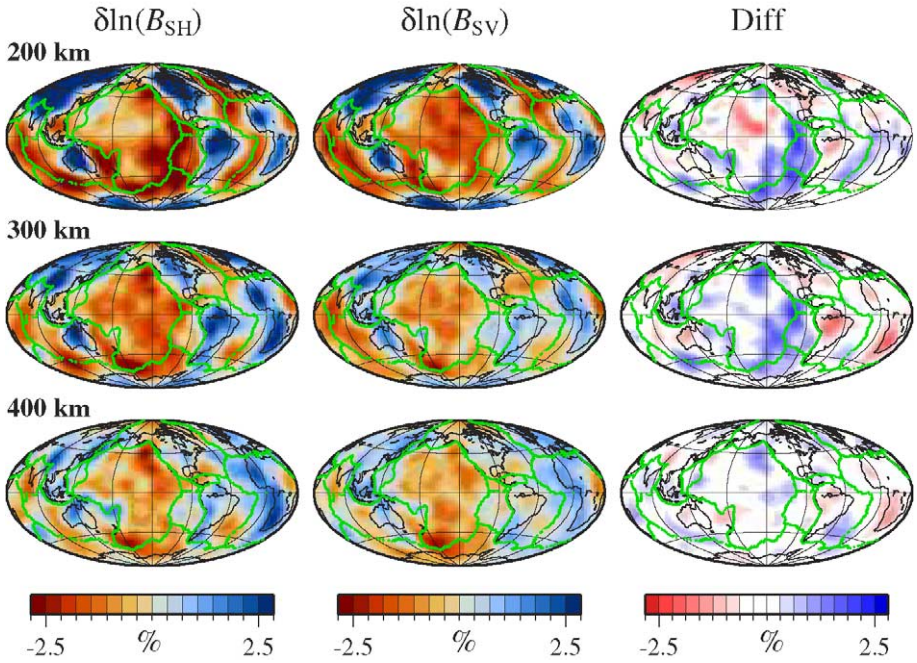


Fig. 4. Anisotropic perturbations $\delta\ln(B_{SH})$ (left), $\delta\ln(B_{SV})$, and their difference $(\delta\ln(B_{SV})-\delta\ln(B_{SH}))$ (right). These two models tend to track each other in the top 300 km, but differences exist beneath the major mid-ocean ridges where the $B_{SH}$ perturbations show a much stronger ridge signature than $B_{SV}$, especially under the EPR. This model shows virtually zero anisotropy at 400 km.

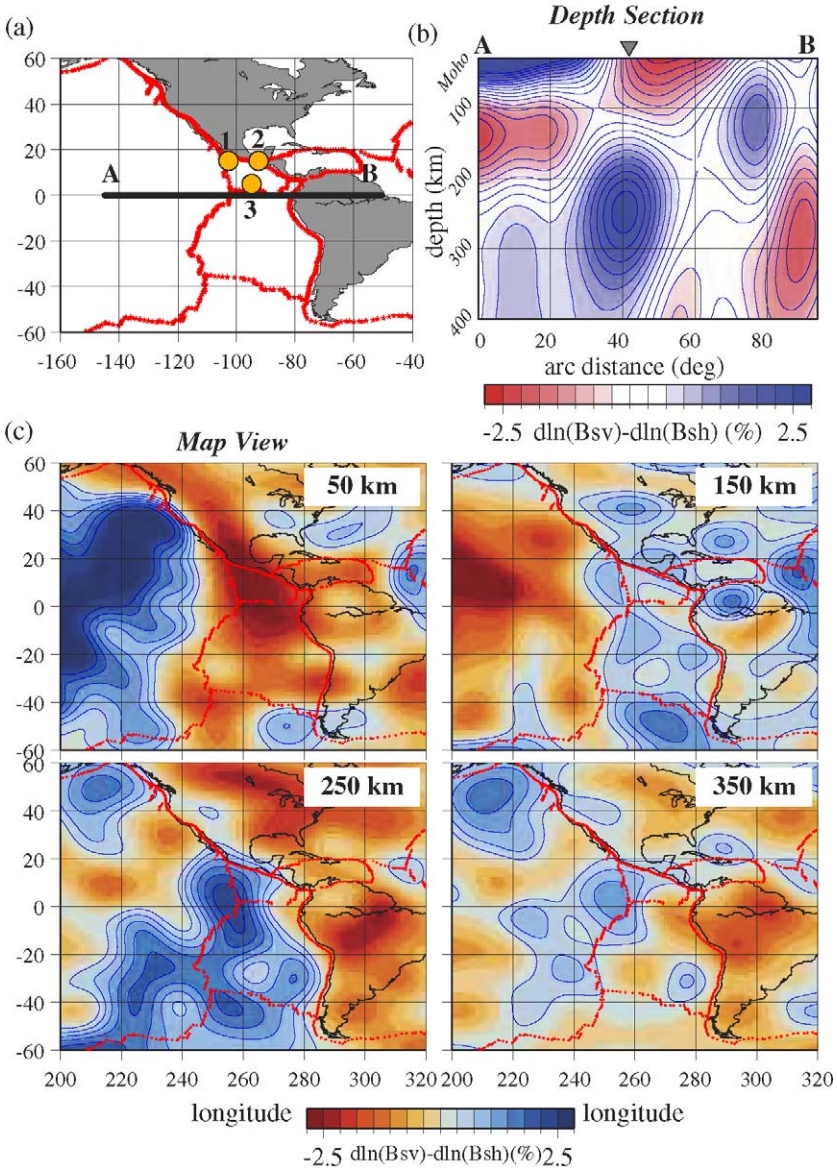


Fig. 5. (a) Map view of the eastern Pacific. The numbered circles indicate the centers of the stacking caps (with 10° radius) for an *SS* precursor analysis (see Section 3.2). (b) A cross section of the anisotropic perturbations (relative to PREM) through the northern EPR. The definition of anisotropy follows that of Fig. 4. We observe two distinct anomalies: a negative ($B_{SH}>B_{SV}$) anomaly above ~100 km, suggesting sub-horizontal foliation planes, and a strong positive anomaly (~2.5%) close to 200 km beneath the surface. The location of the triple junction between the Pacific, Cocos, and Nazca plates is indicated by the inverted triangle. (c) Regional maps of radial anisotropy under the eastern Pacific.

radially. A similar anisotropic pattern is present in Plate 1 of Montagner and Tanimoto [6] and Fig. 3 of a recent global anisotropic inversion by Gung et al. [20], although neither study discussed the robustness and potential implications of this pattern.

We further examine the depth variation of radial anisotropy under the EPR and compare it with that beneath various other ocean basins. Fig. 6a shows the average one-dimensional (1-D) anisotropic wave speeds beneath four different oceanic regions. The

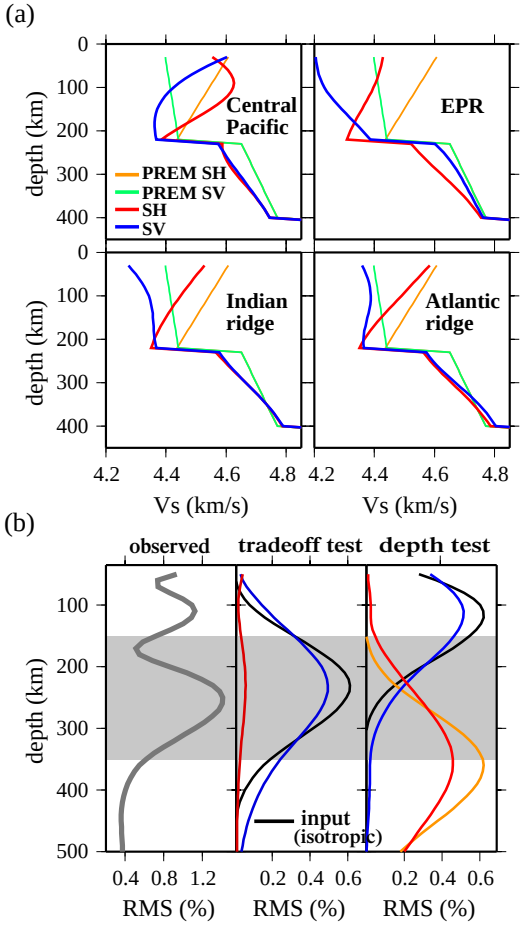


Fig. 6. (a) The average 1D anisotropic wave speeds beneath the central Pacific and global ridge systems. In addition to large differences between $B_{SV}$ and $B_{SH}$ in the top 150 km, the structure beneath the EPR shows substantially greater $B_{SV}$ than $B_{SH}$ in the depth range 200–350 km. (b) Left: Root mean square (RMS) amplitude of anisotropy ($B_{SV}-B_{SH}$) beneath the EPR. The shaded region marks the approximate depth range of the lower-asthenosphere anomaly. Middle: The first set of resolution test. The solid black line shows the RMS of an input anisotropic structure similar to the observed. The blue line shows the recovered RMS using the same data sets and damping scheme. Nearly 75% of the input structure is resolved. In the second test, we construct a purely isotropic input model with the RMS shown by the black curve. The RMS of the output anisotropic variations, shown in red, indicates that the isotropic part of the model only causes minor artifacts to the final anisotropic structure. Right: Depth resolution analysis. In this test, we move the input anisotropy well above (black) and below (brown) the depth of observed anomaly. The output models (blue and red, respectively) recover the peak locations quite well. This suggests that the vertical anisotropy we observe most likely resides within the shaded depth range.

vast regions in central Pacific show nearly zero anisotropy immediately beneath the crust but strong anisotropy in the depth range 100–150 km. This structure was first reported by [19] and corroborated by [20]. The most probable cause is the transition from anisotropy frozen into the cooling oceanic lithosphere to a sub-horizontal flow regime within the asthenosphere immediately below, correlating with present-day plate motion. In contrast, the EPR shows significant anisotropy in the upper 50–100 km, much shallower than beneath the body of the plate. The anisotropic wave speeds converge at ~160 km, below which a significantly faster $B_{SV}$ wave speed (with respect to $B_{SH}$) persists down to ~300 km. This behavior is not clearly observed at slower-spreading ridges, where the averaged $B_{SV}$ and $B_{SH}$ over the entire ridge segments appear to be consistent between 200 and 400 km. The average strength of anisotropy beneath EPR is highlighted by its root mean square (RMS) values with depth (Fig. 6b, left). The positive ($B_{SV}>B_{SH}$), deep asthenospheric anomaly is responsible for the major peak, observed primarily in the shaded region between 150 and 350 km. The secondary peak near 75-km depth results from the negative anomaly ($B_{SH}$—fast) east of the EPR ridge axis. It is worth noting that this shallower peak corresponds to perturbations relative to PREM—a starting model with strong horizontal anisotropy in the top 220 km. When the starting model is included, the absolute anisotropy in the top 120 km (>5%) is larger than that at 230 km [19]. However, regardless of whether absolute or relative wave speed is considered, the RMS variations shown here clearly support a relative simple, two-layered anisotropic structure.

We assess the delineation of the anomalous structure beneath the EPR by tracing rays through an a priori anisotropic model and inverting the synthetic data with identical weighting and smoothing criteria, a standard procedure for determining the resolving power of our data. This test provides a measurable assessment of the seismic illumination of the proposed anomaly (Fig. 6b, middle). The input model contains fast-vertical anisotropy distributed along the entire EPR (Fig. 7), with the maximum amplitude at ~225 km, and is substantially recovered by our inversion. The map inset and cross section of the input model are shown in the left panel. Our

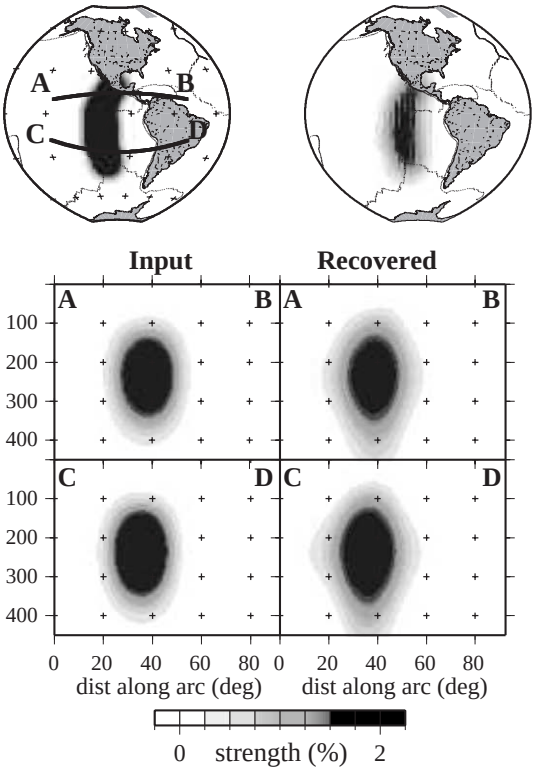


Fig. 7. A resolution test (see Fig. 6b) of an a priori anisotropic anomaly along the EPR. The map inset (at 250-km depth) and cross section of the input model are shown in the left-hand column. The right-hand side shows the resulting model values by inverting for the input anisotropy using the same data sets and smoothing criteria. Our inversion recovers up to 75% of input amplitude.

inversion procedure recovers up to 75% of the input amplitude, and the spatial mislocation of the anomaly is minimal.

We further examine the tradeoff between isotropic and anisotropic perturbations by inverting synthetic data computed from a purely isotropic model using an anisotropic parameterization. The resulting anisotropic artifacts are less than 10% of the input perturbation (see Fig. 6b, middle). We further quantify our ability to constrain the depth dependence of an anisotropic anomaly by inverting synthetic data computed for a sequence of models that place an anisotropic anomaly at different depths (Fig. 6b, right). The results clearly state that the inversion recovers the location of peak amplitude with a depth uncertainty of approximately 50 km.

### 3.2. Mantle reflector

Our data, particularly the long-period mantle waveforms, favor significant vertical anisotropy near 230-km depth beneath the EPR. The strength of the anomaly decays quickly with depth, and the transition to an isotropic depth regime (roughly, 300–400 km) could potentially be associated with a gradient or jump in shear velocity. The existence of mantle discontinuities above 400 km, particularly the Lehmann and 'X' discontinuities (e.g., [30]), is not uniformly established everywhere. Studies of underside reflection or depth phases [31,32], ScS reverberations [8,30], and P-to-S converted waves [17,33–36] have quantified the strong spatial and depth variability of mantle reflectors between 200- and 300-km depths. Mostly observed under continents and island arc regions, these mantle reflector(s) could represent a rheological boundary that demarcates the rigid continental plate from a more plastic, convecting mantle below.

Regional deep asthenospheric discontinuities such as the Lehmann and 'x' discontinuities are not normally associated with mid-ocean ridges. However, a global analysis of the Lehmann discontinuity using *SdS* (*d* for discontinuity; Fig. 8a) stacks [37] provided preliminary evidence for an asthenospheric reflector beneath the northern EPR. This result and the presence of anisotropy motivate a regional search for such a reflector in this region. In the present study, we utilize the broadband mantle waveform data used in the inversions. We form 10° radius stacks of high signal-to-noise ratio seismograms (signal-to-noise ratio >5), and obtain regional transverse-component stacks using a bootstrapping approach [38,39]. The effective lateral resolution of these stacks is approximately 1500 km. The presence of a detectable bottom-side reflection in the resulting stacks of three averaging caps (see yellow circles in Fig. 4a for center locations) reinforces the earlier findings of [37] (Fig. 8b). We clearly identify an anomalous phase, sandwiched between the expected arrivals of *S410S* and *SS*, which corresponds to a bottom-side reflection off a mild asthenospheric reflector. The arrival time of the reflection precedes the 220-km reflection computed using PREM and suggests an average depth close to 260 km. Out of the three stacking bins, cap 3 is the most interesting since the pre-stacked reflections are

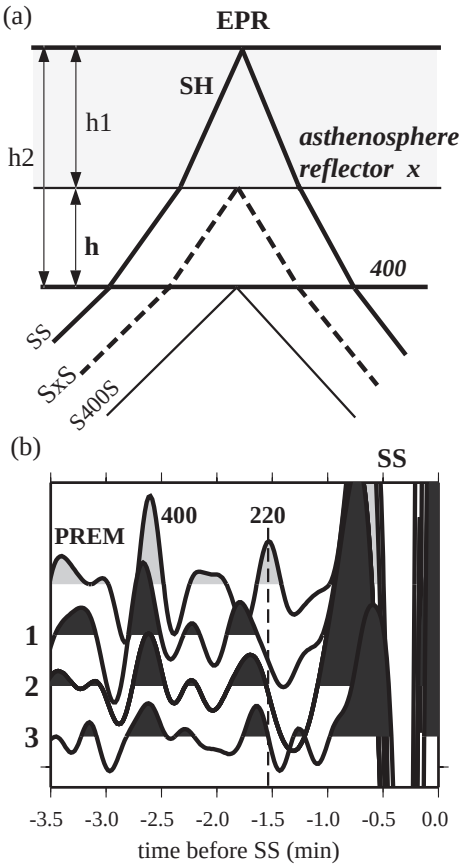


Fig. 8. (a) Ray geometry of underside reflections. (b) Stacked *SS* precursors beneath the EPR. The cap centers are shown in Fig. 5a. The numbers of stacked records are 93, 66, and 23, and the uncertainties based on bootstrapping are 4.4 s, 6.2 s, and 3.6 s, respectively, for caps 1, 2, and 3. The top trace is a stacked synthetic seismogram computed using PREM.

exclusively oceanic. The nature of the 20–30 km topography exhibited by these three caps (see Fig. 8) is still unclear, although the different distances from the cap centers to the slower asthenospheric velocities beneath the northernmost EPR (see Fig. 4) could be partly responsible.

Despite the transverse character of the observed particle motions, the above precursory arrival reflects changes in both $B_{SH}$ and $B_{SV}$ due to the non-vertical ray angles at the reflection points. The positive polarity of the precursor is consistent with the PREM *S220S* pulse, which infers a sharp increase of apparent (a combination of $B_{SH}$ and $B_{SV}$) shear speed with depth that coincides with the lower boundary of the fast-vertical anisotropic anomaly. In fact, the same phase (*SdS*) was used by Lee and Grand [40] to explore the lateral thickness variation of the transition zone (400–700 km) beneath the northern EPR, with many of the reflection points overlapping those of our study. [40] exclusively focused on the thermal imprint of EPR at greater depths, yet their plain (Fig. 5) [40] and slant (Fig. 4) [40] stacks clearly show a coherent seismic phase arriving within 1 min after *S410S*. The delay time of the phase relative to *S410S*, a more robust estimator than the absolute time, is well within the range of our observations (50–60 s).

Further evidence of regional scale, upper mantle reflectors beneath the EPR comes from Shen et al. [41], who show a significant mantle arrival (Fig. 2 of their study) in the MELT region of 18° S at a depth slightly shallower than our interpretation. A direct comparison of our *SdS* stacks with this result is inconclusive owing to the lack of *SdS* data coverage in the southern hemisphere. However, the northern EPR does not appear to be the lone ridge segment under which potential deep asthenospheric reflector(s) exists. Several *SdS* stacks sampling the southern EPR and mid-ocean ridges beneath the Atlantic Ocean (see [39]) contain distinct arrivals between *SS* and *S400S* that could reflect sudden changes in apparent shear velocities between 160-km and 350-km depths. These arrivals are rarely seen in stacks sampling the vast ocean basins away from the ridge axis, most notably in the central Pacific. We need more data to accurately quantify the reflection characteristics beneath young and old oceanic lithospheres.

## 4. Interpretation of anisotropy as horizontal and vertical flow

The main observations of this study can be summarized using a simple cartoon (Fig. 9). Beneath the eastern Pacific, most notably the EPR, the radial anisotropy shifts from a predominantly horizontal orientation in the top 120 km to vertical below 200 km. This deep vertical-fast anisotropic anomaly is a notable departure from the global average PREM anisotropy, which is characterized by large-scale, horizontal alignment of olivine above 220 km and zero anisotropy below it. The strength and location of the anomaly are consistent with the results of [6,20],

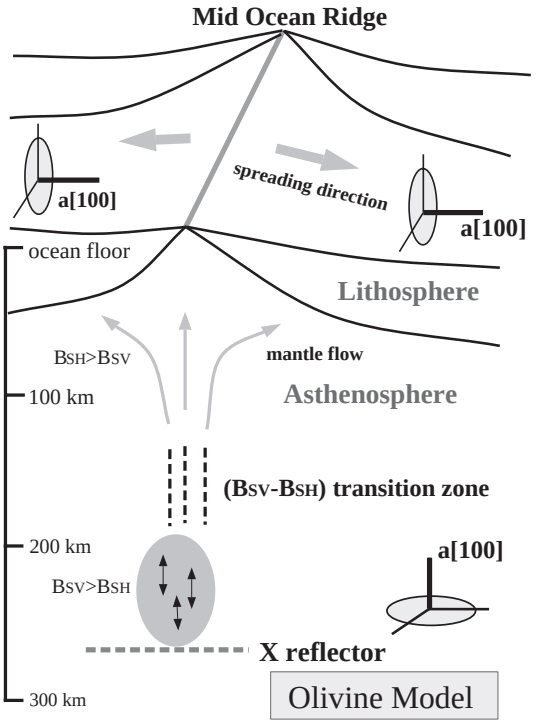


Fig. 9. This figure is modified from [3]. Our observations infer horizontally oriented anisotropy in the top 100 km, vertically oriented anisotropy between 200 and 300 km, and an anomalous mantle reflector near 260 km.

although controversial features within PREM (e.g., the termination depth of anisotropy and a subsequent seismic jump at 220 km) make the interpretation of the anisotropy less intuitive. However, the vertical anisotropic anomaly beneath the EPR appears to be well resolved and independent of the starting model. As evidence of this we compare our result (Fig. 10a) with three recent global studies of anisotropy (Fig. 10b–d), obtained primarily using long-period surface waves. The agreement among these models is significant, in spite of obvious differences in data, modeling philosophy, and parameterization. All four models show strong vertical anisotropy at 250 km beneath the EPR, although the first two models (Fig. 10a and b) used PREM as the starting model and the last two (Fig. 10c and d) did not. Ekström and Dziewonski [19] and Boschi and Ekström [42] used spherical harmonics and 'blocks,' respectively, to represent the lateral variation of anisotropic speeds. Both studies were based on ray-theoretical approximations, whereas Zhou et al. [43] inverted the phase-delay measurements of Laske and Masters [44] relative to 1066A [45] using finite-frequency 3D kernels. The deepest extent of the vertical anisotropy is approximately 300 km, consistent among all four models.

Our result beneath the EPR conforms to PREM-like horizontal flow at shallow depths ($B_{SH}>B_{SV}$), but suggests vertical flow toward the bottom of the asthenosphere. This pattern is repeated beneath only parts of other ridges (see Figs. 4 and 6a), and a systematic discussion of the anomaly with respect to spreading velocity is the subject of a further analysis. In general, the lateral scales of heterogeneities and anisotropy beneath fast-spreading ridges are smaller, but the thermal and compositional variations could potentially be greater than those beneath the continents. The lateral extent of the asthenospheric anomaly is on the order of 300–800 km, accounting for the inherent lateral smoothing due to incomplete data coverage. The depth of our anomaly corroborates with the hypothesis of Evans et al. [46], who analyzed magnetotelluric records from the MELT experiment [23] and raised the possibility of a highly conductive region at approximately 200-km depth west of the EPR. The existence of a deep conductive layer could suggest the presence of partial melt. Deep partial melt situated in vertically aligned channels could account for the fast-vertical anomaly observed in our data, and the crossover of the solidus below the partial melt zone could account for the observed velocity jump at 260 km. We interpret this coincidence as evidence that melt may have, over time, channelized at much greater depths than previously realized.

Even if partial melt is not present at these depths, the depth extent of the fast-vertical anomaly and the 260-km discontinuity may suggest the presence of a rheological change, perhaps related to changes in strain rate, or the average orientation of finite strain. Based on depth alone, this reflector could be quantified as the 'X' discontinuity [31], although it is still unclear whether this discontinuity represents the transitional depth of creep regimes [8,47], a boundary layer of anisotropy induced by asthenospheric flow [19–21], or solid–solid phase transition(s) [48]. The potential presence of water makes it more difficult to accurately quantify the cause of these mild asthenospheric reflector(s) in general.

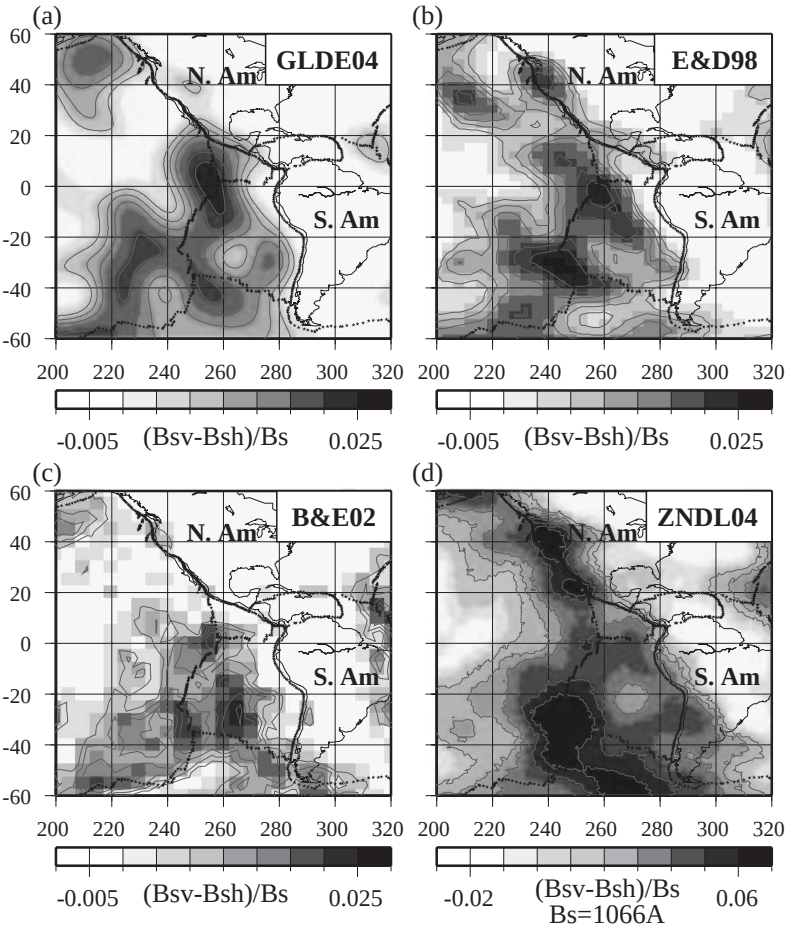


Fig. 10. A comparison of our anisotropic model (GDSE04) at 250 km with three other recent models. E and D98=Ekström and Dziewonski [19]; B and E02=Boschi and Ekström [42]; ZNDL04=Zhou et al. [43]. The pattern of anisotropy near the northern EPR is consistent among all three models.

What we do know is that the depths of the vertical anisotropy and mantle discontinuity are within the upper 200–300 km of the upper mantle. Results from global and regional studies of mantle discontinuities [24,40,41], which are strongly sensitive to thermal variations, have shown little evidence for any significant thermal signature under spreading ridges at depths beneath 400 km. Our re-examination shows that the lateral variation of discontinuity depth under the northern EPR does not stand out from the ambient mantle; the topography is characterized by a modest depression of 2–3 km, well within the uncertainty of the depth measurements (see also [24]). This suggests that it is unlikely that major thermal influences (e.g., upwelling from a deeper mantle source directly beneath the northern part of the EPR) could be responsible for the observed anisotropy and jump in apparent seismic velocity.

The history of melt transport may hold the key to understanding the observed anisotropic pattern. We may think of the 260-km discontinuity as the depth above which mantle flow within the asthenospheric system becomes organized vertically, eventually shifting to dominantly horizontal flow at shallower depths and at greater distances from the ridge. Alternatively, this deep anisotropic signature may also result from 3D deformations associated with horizontal shear, that is, by forming weak and strong

shear zones, a 90° shift of fast direction (to vertical) could potentially take place during the process of melt segregation [49]. The effect of such a mechanism on the vertical shear wave speed will then become less clear. Dense regional data coverage, particularly that achievable from ocean bottom deployments, are needed to confidently differentiate these possible mechanisms.

## Acknowledgement

We thank Barbara Romanowicz and Mark Panning for their scientific help during the formulation of the inverse problem. We also thank Ying Zhou for discussions and for sending their latest anisotropic model of the upper mantle. Lapo Boschi kindly sent us the coefficients of his 2002 anisotropic shear velocity model. This paper also benefited from the constructive comments from Arwen Duess and an anonymous reviewer. Some of the figures were generated using the GMT mapping software [50]. This is Lamont contribution 6721.

## References

[1] A.R. Leeds, L. Knopoff, E.G. Kausel, Variations of upper mantle structure under the Pacific Ocean, Science 186 (1974) 141–143.
[2] B.J. Mitchell, G. Yu, Surface wave dispersion, regionalized velocity models, and anisotropy of the Pacific crust and upper mantle, Geophys. J. R. Astron. Soc. 63 (1980) 497–514.
[3] C.E. Nishimura, D.W. Forsyth, The anisotropic structure of the upper mantle in the Pacific, Geophys. J. R. Astron. Soc. 96 (1989) 203–229.
[4] A.M. Dziewonski, D. Anderson, Preliminary reference Earth model, Phys. Earth Planet. Inter. 25 (1981) 297–356.
[5] D.L. Anderson, Theory of the Earth, Blackwell, 1989, 366 pp.
[6] J.-P. Montagner, T.R. Tanimoto, Global upper mantle tomography of seismic velocities and anisotropies, Geophys. Res. 96 (1991) 20337–20350.
[7] S. Zhang, S. Karato, Lattice preferred orientation of olivine aggregates deformed in simple shear, Nature 375 (1995) 774–777.
[8] J.B. Gaherty, T.H. Jordan, Lehmann discontinuity as the base of an anisotropic layer beneath continents, Science 268 (1996) 1468–1471.
[9] G. Hirth, D.L. Kohlstedt, Water in the oceanic upper mantle; implications for rheology, melt extraction and the evolution of the lithosphere, Earth Planet. Sci. Lett. 144 (1996) 93–108.
[10] C.J. Wolfe, S.C. Solomon, Shear-wave splitting and implications for mantle flow beneath the MELT region of the East Pacific Rise, Science 280 (1998) 1230–1232.
[11] V. Levin, W. Menke, J. Park, Shear-wave splitting in Appalachians and Urals: a case for multilayered anisotropy, J. Geophys. Res. 104 (1999) 17975–17994.
[12] C.E. Hall, K.M. Fischer, E.M. Parmentier, D.K. Blackman, The influence of plate motion on three-dimensional back arc mantle flow and shear wave splitting, J. Geophys. Res. 105 (2000) 28009–28033.
[13] C.A. Curry, J.F. Cassidy, R.D. Hyndman, A regional study of shear wave splitting above the Cascadia subduction zone: margin-parallel crustal stress, Geophys. Res. Lett. 28 (2001) 659–662.
[14] G.H.R. Bokelmann, P. Silver, Shear stress at the base of shield lithosphere, Geophys. Res. Lett. 29 (2002) 23–26.
[15] J. Polet, H. Kanamori, Anisotropy beneath California: shear wave splitting measurements using a dense broadband array, Geophys. J. Int. 149 (2002) 313–317.
[16] D.K. Blackman, M. Kendall, Seismic anisotropy in the upper mantle: 2. Predictions for current plate boundary flow models, Geochem. Geophys. Geosyst. 3 (2002) doi:10.1029/2001GC000247.
[17] J. Park, V. Levin, Seismic anisotropy: tracing plate dynamics in the mantle, Science 296 (2002) 485–489.
[18] S. Chevrot, R.D. van der Hilst, On the effects of a dipping axis of symmetry on shear wave splitting measurements in a transversely isotropic medium, Geophys. J. Int. 152 (2003) 497–505.
[19] G. Ekström, A.M. Dziewonski, The unique anisotropy of the Pacific upper mantle, Nature 394 (1998) 168–172.
[20] Y. Gung, M. Panning, B. Romanowicz, Global anisotropy and the thickness of continents, Nature 422 (2003) 707–711.
[21] J. Plomerova, V. Babuska, L. Vecsey, D. Kouba, Seismic anisotropy of the lithosphere around the Trans-European suture zone (TESZ) based on teleseismic body-wave data of the TOR experiment, Tectonophysics 360 (2002) 89–114.
[22] G. Ekström, J. Tromp, E.W. Larson, Measurements and global models of surface wave propagation, J. Geophys. Res. 102 (1997) 8137–8157.
[23] MELT Seismic Team, Imaging the deep seismic structure beneath a mid-ocean ridge: the MELT experiment, Science 280 (1998) 1215–1218.
[24] Y.J. Gu, A.M. Dziewonski, G. Ekström, Simultaneous inversion for mantle shear velocity and topography of transition zone discontinuities, Geophys. J. Int. 154 (2003) 559–583.
[25] Y.J. Gu, A.M. Dziewonski, W.-J. Su, G. Ekström, Models of the mantle shear velocity and discontinuities in the pattern of lateral heterogeneities, J. Geophys. Res. 106 (2001) 11169–11199.
[26] H.C. Nataf, I. Nakanishi, D.L. Anderson, Anisotropy and shear-velocity heterogeneities in the upper mantle, Geophys. Res. Lett. 11 (1984) 109–112.
[27] J.H. Woodhouse, A note on the calculation of travel times in a transversely isotropic Earth model, Phys. Earth Planet. Inter. 25 (1981) 357–359.

[28] B. Romanowicz, Global mantle tomography: progress status in the past 10 years, Annu. Rev. Earth Planet. Sci. 31 (2003) 303–328.
[29] W. Mooney, G. Laske, T.G. Masters, CRUST 5.1; a global crustal model at 5 degrees×5 degrees, J. Geophys. Res. 103 (1998) 727–747.
[30] J. Revenaugh, T.H. Jordan, A study of mantle layering beneath the western Pacific, J. Geophys. Res. 94 (1989) 5787–5813.
[31] A. Deuss, J.H. Woodhouse, A systematic search for mantle discontinuities using SS precursors, Geophys. Res. Lett. 29 (2002) doi:10.1029/2002GL014768.
[32] J.E. Vidale, H. Benz, Upper-mantle seismic discontinuities and the thermal structure of subduction zones, Nature 356 (1992) 678–683.
[33] M.G. Bostock, A seismic image of the upper mantle beneath the North American Craton, Geophys. Res. Lett. 23 (1996) 1593–1596.
[34] M.G. Bostock, Seismic imaging of lithospheric discontinuities and continental evolution, Lithos 48 (1999) 1–16.
[35] X. Li, G. Bock, A. Vafidis, R. Kind, H.P. Harjes, W. Hanka, K. Wylegalla, M. van der Meijde, X.-H. Yuan, Receiver function study of the Hellenic subduction zone: imaging crustal thickness variations and the oceanic Moho of the descending African lithosphere, Geophys. J. Int. 155 (2003) 733–748.
[36] H. Thybo, E. Perchuc, The seismic 8 degrees discontinuity and partial melting in continental mantle, Science 275 (1997) 1626–1629.
[37] Y.J. Gu, A.M. Dziewonski, G. Ekström, Preferential detection of the Lehmann discontinuity beneath continents, Geophys. Res. Lett. 28 (2001) 4655–4658.
[38] P.M. Shearer, Global mapping of upper mantle reflectors from long-period SS precursors, Geophys. J. Int. 115 (1993) 878–904.
[39] Y.J. Gu, A.M. Dziewonski, Global variability of transition zone thickness, J. Geophys. Res. 107 (2002) doi:10.1029/2002JB000489.
[40] D.K. Lee, S.P. Grand, Depth of the upper mantle discontinuities beneath the East Pacific Rise, Geophys. Res. Lett. 23 (1996) 3369–3372.
[41] Y. Shen, A.-F. Sheehan, K.G. Dueker, C. de-Grot-Hedlin, H. Gilbert, Mantle discontinuity structure beneath the southern East Pacific Rise from P-to-S converted phases, Science 280 (1998) 1232–1235.
[42] L. Boschi, G. Ekström, New images of the Earth's upper mantle from measurements of surface wave phase velocity anomalies, J. Geophys. Res. 107 (2002) doi:10.1029/2000JB000059.
[43] Y. Zhou, G. Nolet, F.A. Dahlen, G. Laske, Global upper-mantle structure from finite-frequency surface-wave tomography, J. Geophys. Res. (submitted for publication).
[44] G. Laske, G. Masters, Constraints on global phase velocity maps from long-period polarization data, J. Geophys. Res. 101 (1996) 16059–16075.
[45] F. Gilbert, A.M. Dziewonski, An application of normal mode theory to the retrieval of structural parameters and source mechanisms from seismic spectra, Philos. Trans. R. Soc. Lond. 278 (1975) 187–269.
[46] R.L. Evans, P. Tarits, A.D. Chave, A. White, G. Heinson, J.H. Filloux, H. Toh, N. Seama, H. Utada, J.R. Booker, M.J. Unsworth, Asymmetric electrical structure in the mantle beneath the East Pacific Rise at 17 degrees S, Science 286 (1999) 752–756.
[47] S. Karato, Importance of anelasticity in the interpretation of seismic tomography, Geophys. Res. Lett. 20 (1993) 1623–1626.
[48] M. Akaogi, H. Yusa, K. Shiraishi, T. Suzuki, Thermodynamic properties of alpha-quartz, coesite, and stishovite and equilibrium phase relations at high pressures and high temperatures, J. Geophys. Res. 100 (1995) 22337–22347.
[49] B.K. Holtzman, D.L. Kohlstedt, M.E. Zimmerman, F. Heidelbach, T. Hiraga, J. Hustoft, Melt segregation and strain partitioning; implications for seismic anisotropy and mantle flow, Science 301 (2003) 1227–1230.
[50] P. Wessel, W.H.F. Smith, Free software helps map and display data, Eos Trans. AGU 72 (441) (1991) 445–446.